THE JOURNAL OF PHYSICAL CHEMISTRY LETTERS
A JOURNAL OF THE AMERICAN CHEMICAL SOCIETY

pubs.acs.org/JPCL

Letter

Size-Scalable Near-Infrared Photoluminescence in Gold Monolayer Protected Clusters

Patrick J. Herbert, Christopher J. Ackerson, and Kenneth L. Knappenberger, Jr.*

Cite This: *J. Phys. Chem. Lett.* 2021, 12, 7531−7536

Read Online

ACCESS | Metrics & More | Article Recommendations | Supporting Information

ABSTRACT: Near-infrared photoluminescence of a series of three gold monolayer protected clusters (MPCs) with volumes spanning 50−200 Å^3 was studied by using variable-temperature photoluminescence (VT-PL) spectroscopy. The three MPCs, which included $Au_{20}(SC_8H_9)_{15}$-diglyme, $Au_{25}(SC_8H_9)_{18}$, and $Au_{38}(SC_{12}H_{25})_{24}$, all exhibited temperature-dependent intensities that reflected a few-millielectronvolt energy gap that separated bright emissive and dark nonradiative electronic states. All clusters showed increased PL intensities upon raising the sample temperature from 4.5 K to a cluster-specific value, upon which increased sample temperature resulted in emission quenching. The increased PL in the low-temperature range is attributed to thermally activated carrier transfer from dark to bright states. The quenching at elevated temperatures is attributed to nonradiative vibrational relaxation through Au−Au stretching of the MPCs metal core. Importantly, the results show evidence of a common and size scalable metal-centered intraband PL mechanism that is general for ultrasmall metal nanoclusters, which are expected to show nonscalable optical properties.

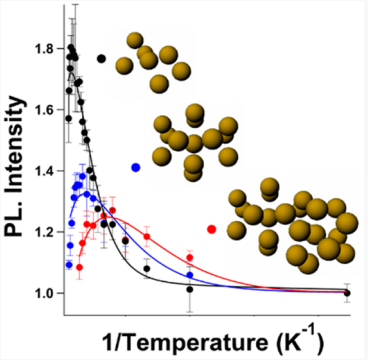

Photoluminescence (PL) by colloidal coinage metals has fascinated chemists for several decades.[1,2] This interest spans length scales, including the ultrasmall, so-called molecular-like nanoclusters and larger, plasmon-supporting nanoparticles. The many potential applications of metal nanoparticle PL include for optical imaging; the PL provides a photostable, nonintermittent photon source.[3,4] Plasmon-mediated PL can be used to generate circular dichroism images of chiral objects.[5] Also, metal PL signals can be analyzed to determine electronic temperatures and resolve energy conversion mechanisms.[6−8] Evidence for both nanoparticle interband- and intraband-based carrier recombination exists.[9] For gold nanorods, intraband emission yields and energies scale with length-to-diameter aspect ratios.[10] Metal nanoclusters also exhibit multiple PL emission bands, which have been attributed to metal−metal-based intraband and interband charge transfer recombination.[9,11,12] Nanocluster emission is often spin polarized, with degrees of polarization that depend on cluster composition and emission energy.[12,13] In contrast to plasmonic nanoparticles, the optical properties of nanoclusters are not believed to be size scalable; PL occurs between discrete cluster-specific electronic states. Here, we provide the first-known description of size-scalable PL properties for a series of gold nanoclusters that include $Au_{20}(SC_8H_9)_{15}$-diglyme, $Au_{25}(SC_8H_9)_{18}$, and $Au_{38}(SC_{12}H_{25})_{24}$. Specifically, we resolve a bright−dark state energy gap that decreases nonlinearly with increasing volume of the metal nanocluster core.

Monolayer-protected clusters (MPCs) are a reliable model system for understanding structure-dependent photoluminescence behavior of metal nanoclusters.[12−17] For thiol-protected gold MPCs, nanoclusters consist of an all-metal core which is protected by gold−chalcogenide semi-rings that are terminated by organic ligands.[18,19] Recently, the photoluminescence mechanism for the charge-neutral $Au_{25}(SC_8H_9)_{18}$ MPC was characterized by using variable-temperature variable field magnetic circular photoluminescence (VTV$\vec{H}$-MCPL) spectroscopy.[12,20] Three PL channels were resolved and assigned through analysis of VTV$\vec{H}$-MCPL and VT-PL methods. A near-infrared PL component was assigned to intraband radiative relaxation involving superatomic states of the metal core. Visible PL components were assigned to core-to-ligand relaxation channels. The relative contributions of each PL channel to the global cluster emission were correlated to transition-specific electronic−vibrational coupling, spin−orbit coupling, and electronic fine-structure energy gaps. The energy gaps associated with near-infrared- and visible-based PL channels were 3.3 meV and ∼600 μeV, respectively. VT-PL studies determined that the temperature-dependent PL intensity and degree of spin polarization were correlated to the magnitude of these fine-structure energy barriers. Notably, the fine-structure barrier associated with the near-infrared, metal core-based intraband PL channel was characterized as the energy separation between a "bright" emissive state and a lower lying "dark" state. This relative energy ordering of the

Received: June 29, 2021
Accepted: July 29, 2021
Published: August 4, 2021

https://doi.org/10.1021/acs.jpclett.1c02100
J. Phys. Chem. Lett. 2021, 12, 7531−7536

electronic states led to increased PL intensity via thermal population transfer from dark to bright states upon increasing the sample temperature from 4.5 K until saturation of the 3.3 meV energy barrier (~60 K). A VT-PL study of the $Au_{24}Pd(SC_8H_9)_{18}$ cluster exhibited qualitatively similar temperature-dependent intensity behavior for the near-infrared PL with notable quantitative differences.[13] The bright−dark energy gap decreased from 3.3 to 1.9 meV, and the emission energy showed an ~40 meV blue-shift upon Pd substitution for gold. These observations support assignment of the NIR PL to metal core-based emission because Pd substitution for Au in $Au_{25}(SC_8H_9)_{18}$ occurs exclusively at core sites.[21]

Here we provide evidence that the temperature-dependent behavior of core-localized intraband PL observed for $Au_{25}(SC_8H_9)_{18}$, where SC_8H_9 refers to phenylethanethiol, is general by expanding the study to include $Au_{38}(SC_{12}H_{25})_{24}$ and $Au_{20}(SC_8H_9)_{15}$-diglyme, where $-SC_{12}H_{25}$ and -diglyme refer to dodecanethiol and diethylene glycol dimethyl ether, respectively. VT-PL measurements on the three-cluster series reveal volume-dependent bright−dark energy gaps, where initial increases in sample temperature from 4.5 K lead to PL intensity increases. Sample temperature increases that exceed the bright−dark energy gap result in nonradiative PL quenching for all three clusters.

Figure 1a shows the near-infrared-to-visible PL spectra of charge-neutral $Au_{25}(SC_8H_9)_{18}$ acquired at samples temperatures of 4.5, 60, and 200 K upon excitation at 3.1 eV. The global PL includes three components in this spectral range, with the most intense emission occurring in the near-infrared,

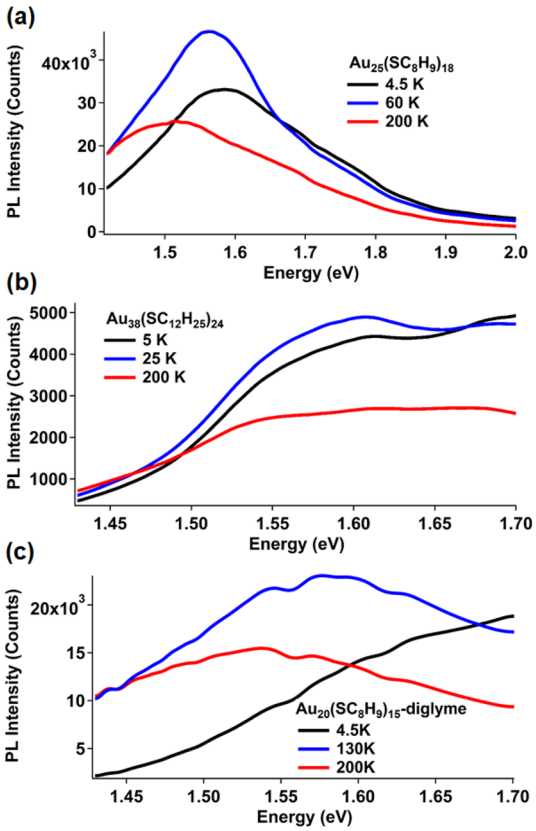

Figure 1. PL spectra of (a) $Au_{25}(SC_8H_9)_{18}$, (b) $Au_{38}(SC_{12}H_{25})_{24}$, and (c) $Au_{20}(SC_8H_9)_{15}$-diglyme at various sample temperatures ranging from 4.5 to 200 K upon 3.1 eV excitation.

at energies typically less than 1.7 eV.[12] As previously reported, an intensity increase of the near-infrared PL is observed upon increasing sample temperature from 4.5 to 60 K.[11,12] Further temperature increases lead to PL quenching due to phonon-mediated nonradiative decay. The near-infrared PL is assigned to intraband relaxation between core-localized states.[11,12,17] Figures 1b and 1c show the PL spectra of the lowest energy PL component of $Au_{38}(SC_{12}H_{25})_{24}$ and $Au_{20}(SC_8H_9)_{15}$-diglyme at various sample temperatures ranging from 4.5 to 200 K, respectively. Similar to $Au_{25}(SC_8H_9)_{18}$, an increase in the near-infrared PL intensity of both $Au_{38}(SC_{12}H_{25})_{24}$ and $Au_{20}(SC_8H_9)_{15}$-diglyme was observed as the sample temperature was increased from 4.5 K, with subsequent emission quenching for thermal energies that exceeded cluster-specific values.

To quantify the energy barriers associated with the temperature-dependent PL intensity behaviors, the integrated intensities of the near-infrared PL were determined for each cluster. Several controls to ensure the PL analysis reflected the properties of isolated (i.e., nonaggregated) gold MPCs are provided in Figures S1−S8. As shown in Figures S1 and S2, dimerization and aggregation induce distinct optical signatures of electronic coupling. This signature allows for both identification of multimers and spectral filtering of isolated MPC emission by data collection at energies less than 1.7 eV. In addition, analysis of the polymer thin film used to prepare the MPC samples does not exhibit any detectable PL emission at energies lower than 1.7 eV. Hence, analysis of PL photons acquired at energies less than 1.7 eV enables analysis of analysis of isolated MPC-specific emission.

Focusing on isolated MPCs, the near-infrared PL components for $Au_{20}(SC_8H_9)_{15}$-diglyme, $Au_{25}(SC_8H_9)_{18}$, and $Au_{38}(SC_{12}H_{25})_{24}$ were fit to single Gaussian functions centered at 1.62 ± 0.01, 1.59 ± 0.01, and 1.58 ± 0.01 eV, respectively; average values and standard deviations are determined from statistical analysis of five trials. Figure 2a shows the integrated PL intensities of $Au_{20}(SC_8H_9)_{15}$-diglyme, $Au_{25}(SC_8H_9)_{18}$, and $Au_{38}(SC_{12}H_{25})_{24}$, normalized to 4.5 K values, plotted versus sample temperature. As the sample temperature is increased from 4.5 K, the PL intensity increases for all clusters. Sample temperatures where the maximal PL intensity is observed are cluster-specific. The maximal PL intensity for $Au_{20}(SC_8H_9)_{15}$-diglyme, $Au_{25}(SC_8H_9)_{18}$, and $Au_{38}(SC_{12}H_{25})_{24}$ was observed at sample temperatures of approximately 130, 60, and 25 K, respectively. At these sample temperatures, the relative increase in PL intensity compared to 4.5 K for $Au_{20}(SC_8H_9)_{15}$-diglyme, $Au_{25}(SC_8H_9)_{18}$, and $Au_{38}(SC_{12}H_{25})_{24}$ was approximately 80%, 38%, and 27%, respectively, reflecting a monotonically decreasing trend with increasing cluster metal volume. The PL intensity for each cluster decreased for sample temperature increases beyond these cluster-specific threshold.

Similar temperature-dependent PL intensity behavior has been observed in a variety of chemical systems.[22−24] One explanation for this temperature-dependent PL behavior is the presence of a spectroscopically dark state, lower in energy relative to the bright emissive state. At 4.5 K, the Boltzmann population preferentially occupies the lower energy dark state. As the sample temperatures increase from 4.5 K, a thermal population redistribution from the low-lying dark state to a bright emissive state occurs. This increase in bright state occupancy results in an increase in PL intensity. As a result, the temperature dependence of PL intensity is correlated to the relative energy separation between bright and dark states. To

https://doi.org/10.1021/acs.jpclett.1c02100
J. Phys. Chem. Lett. 2021, 12, 7531−7536

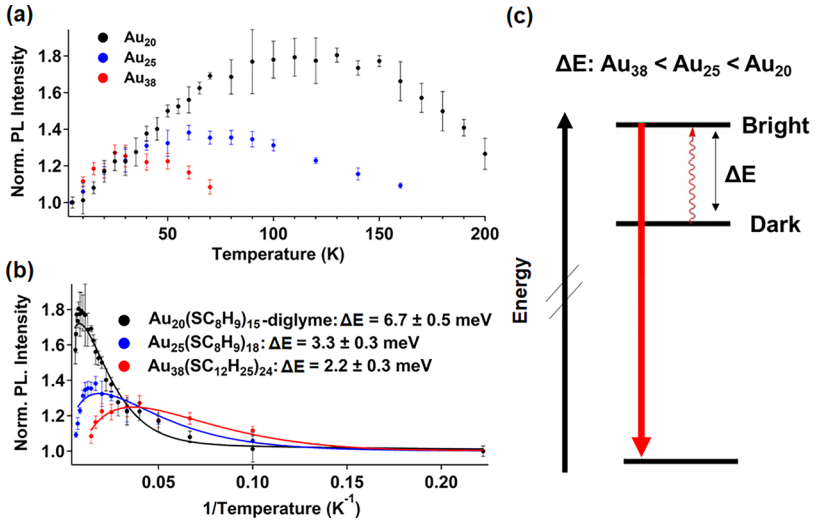

Figure 2. (a) Temperature-dependent integrated PL intensity of $Au_{20}(SC_8H_9)_{15}$-diglyme (black), $Au_{25}(SC_8H_9)_{18}$ (blue), and $Au_{38}(SC_{12}H_{25})_{24}$ (red) normalized at 4.5 K. (b) Temperature-dependent (plotted as reciprocal temperature) PL intensities fit to eq 1 with determined energy difference (ΔE) separating bright and dark states. (c) Schematic of bright−dark state diagram.

quantify the energy separation between the bright and dark states, the temperature-dependent integrated intensity is modeled as a two-level Boltzmann distributed system given by eq 1[25]

$$I(T) = \left(\frac{1}{\sqrt{T}}\right)\left(\frac{m + ne^{-\Delta E/k_B T}}{1 + e^{-\Delta E/k_B T}}\right) + A \quad (1)$$

Here, T is the sample temperature, k_B is the Boltzmann constant, ΔE is the energy separation between bright and dark states (Figure 2c), n and m are spectral weighting factors for the bright and dark state, respectively, and A is a plateau function. Figure 2b shows the resulting fit of the integrated intensity with eq 1. Fitting results from five trials for $Au_{38}(SC_{12}H_{25})_{24}$, $Au_{25}(SC_8H_9)_{18}$, and $Au_{20}(SC_8H_9)_{15}$-diglyme yielded energy barriers with averages and standard deviations of 2.4 ± 0.3, 3.3 ± 0.3, and 6.7 ± 0.5 meV, respectively. Figure 2c depicts the cluster-specific bright−dark state energy separation that gives rise to the observed temperature-dependent behavior. The 3.3 meV energy separation for $Au_{25}(SC_8H_9)_{18}$ is in agreement with core-based fine structure splitting values determined from state-resolved variable-temperature variable-field magnetic circular photoluminescence (VTV$\vec{H}$-MCPL) studies.[12] Theoretical electronic structure calculations of $Au_{25}(SR)_{18}$, where -SR refers to thiolate ligands, are also consistent with our experimental results. These calculations predict fine-structure splitting of the core-based state to be on the order of a few to tens of millielectronvolts.[16,26,27] Transitions between core-based states are predicted to arise near the HOMO−LUMO gap.[16,26,27] The determination of a few millielectronvolts energy barriers to the lowest energy PL component for $Au_{20}(SC_8H_9)_{15}$-diglyme and $Au_{38}(SC_{12}H_{25})_{24}$ implicates similar core-based intraband radiative relaxation for all three clusters. We note that $Au_{25}(SC_8H_9)_{18}$ can be formed in multiple charge states, with 0 and −1 being the most common. The neutral and anionic forms do show distinct HOMO−LUMO energy gaps, and the energy gaps measured here could differ with charge state. The current experimental setup precludes measurements of the anionic clusters and our values are specific to the charge-neutral species.

Previous VT-PL studies have correlated PL intensity to the magnitude of electronic−vibrational coupling to structure-specific modes.[11−13] Characterization of pathway-specific electronic−vibrational coupling is achieved by modeling the temperature-dependent Stokes shift of each PL component by using eq 2[28]

$$E_g(T) = E_g(0) - S\hbar\omega\left[\coth\left(\frac{\hbar\omega}{2k_B T}\right) - 1\right] \quad (2)$$

Here, $E_g(0)$ is the mean peak energy at T = 0, S is the dimensionless coupling constant, $\hbar$ is Planck's constant, and ω is the vibrational angular frequency. As mentioned above, the central peak energies, determined by Gaussian fitting, for the lowest energy PL component for $Au_{20}(SC_8H_9)_{15}$-diglyme, $Au_{25}(SC_8H_9)_{18}$, and $Au_{38}(SC_{12}H_{25})_{24}$ were 1.62 ± 0.01, 1.59 ± 0.01, and 1.58 ±0.01 eV, respectively. Figure 3 shows the temperature-dependent peak energy shifts relative to 4.5 K and fit to eq 2. Table 1 summarizes the fitting results. The vibrational energies ($\hbar\omega$) determined for $Au_{20}(SC_8H_9)_{15}$-diglyme, $Au_{25}(SC_8H_9)_{18}$, and $Au_{38}(SC_{12}H_{25})_{24}$ were 14.5 ± 0.3, 19.1 ± 0.1, and 13.1 ± 0.5 meV, respectively. The coupling constants for the $Au_{20}(SC_8H_9)_{15}$-diglyme, $Au_{25}(SC_8H_9)_{18}$, and $Au_{38}(SC_{12}H_{25})_{24}$ were 5.7 ± 0.2, 4.00 ± 0.04, and 1.95 ± 0.02, respectively.

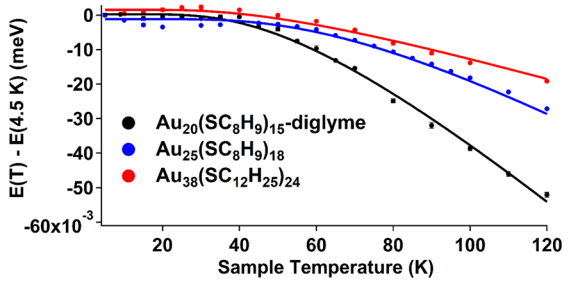

Figure 3. Temperature-dependent peak energy shifts relative to 4.5 K for $Au_{20}(SC_8H_9)_{15}$-diglyme (black), $Au_{25}(SC_8H_9)_{18}$ (blue), and $Au_{38}(SC_{12}H_{25})_{24}$ (red).

https://doi.org/10.1021/acs.jpclett.1c02100
J. Phys. Chem. Lett. 2021, 12, 7531−7536

Table 1. Electronic−Vibrational Coupling Results for $Au_{20}(SC_8H_9)_{15}$-Diglyme, $Au_{25}(SC_8H_9)_{18}$, and $Au_{38}(SC_{12}H_{25})_{24}$

MPC	coupling constant, S	vib energy (meV)
$Au_{20}(SC_8H_9)_{15}$-diglyme	5.7 ± 0.2	14.5 ± 0.3
$Au_{25}(SC_8H_9)_{18}$	4.00 ± 0.04	19.1 ± 0.1
$Au_{38}(SC_{12}H_{25})_{24}$	1.95 ± 0.02	13.1 ± 0.5

The difference in vibrational modes can be understood by differences in the core structure for each cluster. For $Au_{25}(SC_8H_9)_{18}$, the core is composed of a spherically approximated 13 Au atom icosahedron.[19] $Au_{20}(SC_8H_9)_{15}$-diglyme and $Au_{38}(SC_{12}H_{25})_{24}$ exhibit nonspherical, rodlike icosahedral cores.[29,30] The 19.1 meV vibrational mode for $Au_{25}(SC_8H_9)_{18}$ is in agreement with a symmetric radial core breathing mode, whereas the ∼14 meV mode for $Au_{20}(SC_8H_9)_{15}$-diglyme and $Au_{38}(SC_{12}H_{25})_{24}$ agrees with an Au−Au core stretching mode.[31,32] Similar modes are detected in transient absorption data of $Au_{20}(SR)_{16}$.[33] Oscillatory features in transient signal decay with a frequency of 101.7 cm^{-1} (12.6 meV), similar to the value we measure from VT-PL, are observed.[33] This oscillatory frequency was assigned to Au−Au core stretching of the seven-atom core.[33] Hence, the phonon modes implicated in the nonradiative decay (i.e., near-infrared PL quenching) for all clusters can be assigned to vibrations of the metal core. The magnitude of electronic−vibrational coupling obtained from analysis of VT-PL data was also cluster-specific. Electronic−vibrational coupling was observed to increase with decreasing cluster size ($Au_{38}(SC_{12}H_{25})_{24}$ < $Au_{25}(SC_8H_9)_{18}$ < $Au_{20}(SC_8H_9)_{15}$-diglyme). Theoretically calculated Raman spectra for a series of clusters ranging from Au = 4 to Au = 25 determined increasing amplitude of low-energy core localized modes with decreasing cluster size.[31] Similar behavior has been observed in spherical CdSe quantum dots (QD) where decreasing volume results in increased electron−phonon coupling.[34] Taken together, the generalizable bright−dark energy gaps and size-dependent trends in cluster-specific electron−phonon coupling to core-based vibration support the interpretation that the near-infrared emission for the MPCs was due to metal-centered intraband relaxation.

Next, quantitative comparison of MPC-specific trends in near-infrared PL emission to cluster core volume is discussed. Core volumes for $Au_{38}(SC_{12}H_{25})_{24}$, $Au_{25}(SC_8H_9)_{15}$, and $Au_{20}(SC_8H_9)_{15}$-diglyme were approximated from X-ray crystallographic structures as 200, 100, and 50 $Å^3$, respectively.[19,29,30] Figure 4 shows the bright and dark state energy separation, obtained from fitting Figure 2 data to eq 1, for $Au_{20}(SC_8H_9)_{15}$-diglyme, $Au_{25}(SC_8H_9)_{18}$, and $Au_{38}(SC_{12}H_{25})_{24}$. The energy separation decreases nonlinearly (modeled here as a single exponent) with increasing cluster core volume. We note that while we anticipate the energy separation approaches zero for larger core volumes, the sample size studied here limits the determination of the minimum volume. Hence, we attribute this observation to confinement effects associated with the volume of the all-metal-atom core of the cluster. Similar volume-dependent bright−dark energy gaps are known for colloidal semiconductor nanocrystals and nanorods, such as CdSe.[35,36] An important point to note, in the case of the metal nanoclusters studied here, is that the volume-dependent bright−dark energy gap is general with regard to cluster shape and passivating ligand. The energy gap scales with

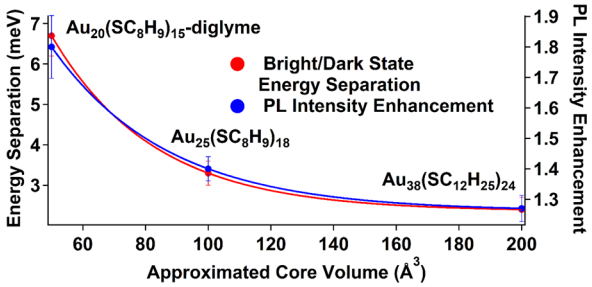

Figure 4. Bright and dark state energy separation (red) and relative PL intensity enhancement factors relative to 4.5 K (blue) for $Au_{20}(SC_8H_9)_{15}$-diglyme, $Au_{25}(SC_8H_9)_{18}$, and $Au_{38}(SC_{12}H_{25})_{24}$ plotted versus approximated core volume.

volume, regardless of a nearly spherical or rodlike shape or choice of the passivating ligand. One explanation for this behavior is the increased density of states that occurs with increasing cluster volume. These observations support our assignment of near-infrared emission to metal-centered and core-localized intraband emission. The origin of bright and dark states could be due to differences in spin−orbit coupling[12] but could also be the result of different symmetries of the electronic states that render the lowest energy state nonemissive.[11,16,37]

The magnitude of the bright−dark state energy separation may have a significant influence on the global PL properties of MPCs. Branching ratio analysis of VT-PL intensities for $Au_{25}(SC_8H_9)_{18}$ and $Au_{24}Pd(SC_8H_9)_{18}$ determined the brightest (highest PL QY) configuration for both clusters corresponded to the greatest partitioning of global PL through core-based intraband relaxation rather than core-to-ligand charge-transfer relaxation.[11−13] Figure 4 also shows the relative PL intensity enhancement factors for each cluster relative to 4.5 K. The relative increase in near-infrared PL intensity scales in agreement with quantified bright−dark state energy separation. However, as previously demonstrated through single Pd atom substitution to $Au_{25}(SC_8H_9)_{18}$, the energy barrier may also be modified through compositional methods.[13] This compositional dependence may also impact spin-polarized PL by MPCs; $Au_{25}(SC_8H_9)_{18}$ exhibits degrees of circularly polarized (DOCP) PL that track with similar temperature dependences as integrated emission intensities.[12] Hence, synthetic modifications that alter the bright−dark energy barrier may allow optimization of MPCs for spin-polarized photonic applications.

In summary, core-localized intraband PL relaxation has been observed and characterized for $Au_{20}(SC_8H_9)_{15}$-diglyme, $Au_{25}(SC_8H_9)_{18}$, and $Au_{38}(SC_{12}H_{25})_{24}$. The low-temperature (<150 K) near-infrared PL intensity behavior is largely dependent on the energy separation between the bright emissive state and a low-lying dark state which is present in all clusters. The energy separation, and consequently maximal intraband PL intensity, increases with decreasing cluster core volume ($Au_{38}(SC_{12}H_{25})_{24}$ < $Au_{25}(SC_8H_9)_{18}$ < $Au_{20}(SC_8H_9)_{15}$-diglyme). Importantly, the results implicate a common, size-scalable mechanism for near-infrared metal nanocluster PL emission.

■ EXPERIMENTAL METHODS

The synthetic protocols for $Au_{20}(SC_8H_9)_{15}$-diglyme, $Au_{25}(SC_8H_9)_{18}$, and $Au_{38}(SC_{12}H_{25})_{24}$ are detailed elsewhere.[38−40] Samples of each cluster were dissolved in a solution of 17% w polystyrene/toluene. The solutions were

https://doi.org/10.1021/acs.jpclett.1c02100
J. Phys. Chem. Lett. 2021, 12, 7531−7536

then dropcast onto a quartz coverslip and placed into a vacuum desiccator to dry. The film serves to prevent desorption of the solid MPC sample under ultrahigh vacuum. Sample slides were affixed to a fiber-optic-containing probe, inserted under vacuum, and cooled to 4.5 K. Control over the sample temperature was maintained through a resistive heater mounted in the probe, giving ∼1% temperature uniformity over the excitation area. Excitation was achieved by using the 3.10 eV frequency-doubled output of a regeneratively amplified Ti:sapphire laser system (Legend, Coherent), producing laser pulses ∼100 fs in duration centered at 1.55 eV. The 3.10 eV pulses were attenuated to 800 nJ/pulse and aligned onto the sample. The resulting photoluminescence was collected with a fiber optic in transmission geometry. Long pass filters set at 2.3 eV were used to isolate the PL from the principal excitation source. Finally, the PL photons were sent to a spectrometer (Princeton Instruments) which spectrally dispersed the emission onto a liquid nitrogen cooled 1340-pixel CCD array (Pylon).

■ ASSOCIATED CONTENT

Supporting Information

The Supporting Information is available free of charge at https://pubs.acs.org/doi/10.1021/acs.jpclett.1c02100.

Figures S1−S8 (PDF)

■ AUTHOR INFORMATION

Corresponding Author

Kenneth L. Knappenberger, Jr. − *Department of Chemistry, The Pennsylvania University, University Park, Pennsylvania 16802, United States;* orcid.org/0000-0003-4123-3663; Email: klk260@psu.edu

Authors

Patrick J. Herbert − *Department of Chemistry, The Pennsylvania University, University Park, Pennsylvania 16802, United States*

Christopher J. Ackerson − *Department of Chemistry, Colorado State University, Fort Collins, Colorado 80523, United States;* orcid.org/0000-0001-6863-6054

Complete contact information is available at: https://pubs.acs.org/10.1021/acs.jpclett.1c02100

Notes

The authors declare no competing financial interest.

■ ACKNOWLEDGMENTS

This work was supported by awards from the National Science Foundation to K.L.K. under Grants CHE-1806222/CHE-1904876 and CHE-1807999. In addition, this work was supported by awards from the National Science Foundation to C.J.A. under Grants CHE-1905179 and CHE-1507646.

■ REFERENCES

(1) Mooradian, A. Photoluminescence of Metals. *Phys. Rev. Lett.* **1969**, *22*, 185−187.

(2) Apell, P.; Monreal, R.; Lundqvist, S. Photoluminescence of Noble Metals. *Phys. Scr.* **1988**, *38*, 174−179.

(3) Sönnichsen, C.; Alivisatos, A. P. Gold Nanorods as Novel Nonbleaching Plasmon-Based Orientation Sensors for Polarized Single-Particle Microscopy. *Nano Lett.* **2005**, *5*, 301−304.

(4) Wang, H.; Huff, T. B.; Zweifel, D. A.; He, W.; Low, P. S.; Wei, A.; Cheng, J. X. In Vitro and in Vivo Two-Photon Luminescence Imaging of Single Gold Nanorods. *Proc. Natl. Acad. Sci. U. S. A.* **2005**, *102*, 15752−15756.

(5) Jarrett, J. W.; Zhao, T.; Johnson, J. S.; Liu, X.; Nealey, P. F.; Vaia, R. A.; Knappenberger, K. L. Plasmon-Mediated Two-Photon Photoluminescence-Detected Circular Dichroism in Gold Nanosphere Assemblies. *J. Phys. Chem. Lett.* **2016**, *7*, 765−770.

(6) Cai, Y.-Y.; Liu, J. G.; Tauzin, L. J.; Huang, D.; Sung, E.; Zhang, H.; Joplin, A.; Chang, W.-S.; Nordlander, P.; Link, S. Photoluminescence of Gold Nanorods: Purcell Effect Enhanced Emission from Hot Carriers. *ACS Nano* **2018**, *12*, 976−985.

(7) Zhao, T.; Li, Z.; Park, K.; Vaia, R. A.; Knappenberger, K. L. Photoluminescence of Single Gold Nanorods Following Nonlinear Excitation. *J. Chem. Phys.* **2020**, *153*, 061101−7.

(8) Sivan, Y.; Dubi, Y. Theory of "Hot" Photoluminescence from Drude Metals. *ACS Nano* **2021**, *15*, 8724−8732.

(9) Link, S.; Beeby, A.; FitzGerald, S.; El-Sayed, M. A.; Schaaff, T. G.; Whetten, R. L. Visible to Infrared Luminescence from a 28 Atom Gold Cluster. *J. Phys. Chem. B* **2002**, *106*, 3410−3415.

(10) Chang, W.-S.; Willingham, B.; Slaughter, L. S.; Dominguez-Medina, S.; Swanglap, P.; Link, S. Radiative and Nonradiative Properties of Single Plasmonic Nanoparticles and Their Assemblies. *Acc. Chem. Res.* **2012**, *45*, 1936−1945.

(11) Green, T. D.; Yi, C.; Zeng, C.; Jin, R.; McGill, S.; Knappenberger, K. L. Temperature-Dependent Photoluminescence of Structurally-Precise Quantum-Confined $Au_{25}(SC_8H_9)_{18}^0$ and $Au_{38}(SC_{12}H_{25})_{24}$ Metal Nanoparticles. *J. Phys. Chem. A* **2014**, *118*, 10611−10621.

(12) Herbert, P. J.; Knappenberger, K. L. Spin-Polarized Photoluminescence in $Au_{25}(SC_8H_9)_{18}$ Monolayer-Protected Clusters. *Small* **2021**, *17*, 2004431.

(13) Herbert, P. J.; Tofanelli, M. A.; Ackerson, C. J.; Knappenberger, K. L. The Influence of Pd-atom Substitution on $Au_{25}(SC_8H_9)_{18}$ Cluster Photoluminescence. *J. Phys. Chem. C* **2021**, *125*, 7267−7275.

(14) Bigioni, T. P.; Whetten, R. L.; Dag, Ö. Near-Infrared Luminescence from Small Gold Nanocrystals. *J. Phys. Chem. B* **2000**, *104*, 6983−6986.

(15) Wu, Z.; Jin, R. On the Ligand's Role in the Fluorescence of Gold Nanoclusters. *Nano Lett.* **2010**, *10*, 2568−2573.

(16) Dimuthu, K. L.; Weerawardene, M.; Aikens, C. M. Theoretical Insights into the Origin of Photoluminescence of $Au_{25}(SR)_{18}^-$ Nanoparticles. *J. Am. Chem. Soc.* **2016**, *138*, 11202−11210.

(17) Green, T. D.; Herbert, P. J.; Yi, C.; Zeng, C.; McGill, S.; Jin, R.; Knappenberger, K. L. Characterization of Emissive States for Structurally Precise $Au_{25}(SC_8H_9)_{18}^0$ Monolayer-Protected Gold Nanoclusters Using Magnetophotoluminescence Spectroscopy. *J. Phys. Chem. C* **2016**, *120*, 17784−17790.

(18) Jadzinsky, P. D.; Calero, G.; Ackerson, C. J.; Bushnell, D. A.; Kornberg, R. D. Structure of a Thiol Monolayer-Protected Gold Nanoparticle at 1.1 Å Resolution. *Science* **2007**, *318*, 430−433.

(19) Zhu, M.; Aikens, C. M.; Hollander, F. J.; Schatz, G. C.; Jin, R. Correlating the Crystal Structure of A Thiol-Protected Au_{25} Cluster and Optical Properties. *J. Am. Chem. Soc.* **2008**, *130*, 5883−5885.

(20) Herbert, P. J.; Mitra, U.; Knappenberger, K. L. Variable-Temperature Variable-Field Magnetic Circular Photoluminescence (VTVH-MCPL) Spectroscopy for Electronic-Structure Determination in Nanoscale Chemical Systems. *Opt. Lett.* **2017**, *42*, 4833−4836.

(21) Tofanelli, M. A.; Ni, T. W.; Phillips, B. D.; Ackerson, C. J. Crystal Structure of the $PdAu_{24}(SR)_{18}^0$ Superatom. *Inorg. Chem.* **2016**, *55*, 999−1001.

(22) Shibata, H. Negative Thermal Quenching Curves in Photoluminescence of Solids. *Jpn. J. Appl. Phys.* **1998**, *37*, 550−553.

(23) Srivastava, A.; Htoon, H.; Klimov, V. I.; Kono, J. Direct Observation of Dark Excitons in Individual Carbon Nanotubes. *Phys. Rev. Lett.* **2008**, *101*, 087402−4.

(24) Shaver, J.; Kono, J. Temperature-Dependent Magneto-Photoluminescence Spectroscopy of Carbon Nanotubes: Evidence for Dark Excitons. *Laser & Photon. Rev.* **2007**, *1*, 260−274.

(25) Mortimer, I. B.; Nicholas, R. J. Role of Bright and Dark Excitons in the Temperature-Dependent Photoluminescence of Carbon Nanotubes. *Phys. Rev. Lett.* **2007**, *98*, 027404−4.
(26) Aikens, C. M. Electronic Structure of Ligand-Passivated Gold and Silver Nanoclusters. *J. Phys. Chem. Lett.* **2011**, *2*, 99−104.
(27) Jiang, D.; Kühn, M.; Tang, Q.; Weigend, F. Superatomic Orbitals under Spin-Orbit Coupling. *J. Phys. Chem. Lett.* **2014**, *5*, 3286−3289.
(28) O'Donnell, K. P.; Chen, X. Temperature Dependence of Semiconductor Band Gaps. *Appl. Phys. Lett.* **1991**, *58*, 2924−2926.
(29) Qian, H.; Eckenhoff, W. T.; Zhu, Y.; Pintauer, T.; Jin, R. Total Structure Determination of Thiolate-Protected Au_{38} Nanoparticles. *J. Am. Chem. Soc.* **2010**, *132*, 8280−8281.
(30) Zeng, C.; Liu, C.; Chen, Y.; Rosi, N. L.; Jin, R. Gold−Thiolate Ring as a Protecting Motif in the $Au_{20}(Sr)_{16}$ Nanocluster and Implications. *J. Am. Chem. Soc.* **2014**, *136*, 11922−11925.
(31) Tlahuice-Flores, A.; Whetten, R. L.; Jose-Yacaman, M. Vibrational Normal Modes of Small Thiolate-Protected Gold Clusters. *J. Phys. Chem. C* **2013**, *117*, 12191−12198.
(32) Nieto-Ortega, B.; Bürgi, T. Vibrational Properties of Thiolate-Protected Gold Nanoclusters. *Acc. Chem. Res.* **2018**, *51*, 2811−2819.
(33) Zhou, M.; Vdović, S.; Long, S.; Zhu, M.; Yan, L.; Wang, Y.; Niu, Y.; Wang, X.; Guo, Q.; Jin, R.; Xia, A. Intramolecular Charge Transfer and Solvation Dynamics of Thiolate-Protected $Au_{20}(SR)_{16}$ Clusters Studied by Ultrafast Measurement. *J. Phys. Chem. A* **2013**, *117*, 10294−10303.
(34) Kelley, A. M. Electron-Phonon Coupling in CdSe Nanocrystals from an Atomistic Phonon Model. *ACS Nano* **2011**, *5*, 5254−5262.
(35) Furis, M.; Htoon, H.; Petruska, M. A.; Klimov, V. I.; Barrick, T.; Crooker, S. A. Bright-Exciton Fine Structure and Anisotropic Exchange in CdSe Nanocrystal Quantum Dots. *Phys. Rev. B: Condens. Matter Mater. Phys.* **2006**, *73*, 241313−4.
(36) Blumling, D. E.; McGill, S.; Knappenberger, K. L. The Influence of Applied Magnetic Fields on the Optical Properties of Zero- and One-Dimensional CdSe Nanocrystals. *Nanoscale* **2013**, *5*, 9049−9056.
(37) Li, Q.; Zeman, C. J.; Ma, Z.; Schatz, G. C.; Gu, X. W. Bright NIR-II Photoluminescence in Rod-Shaped Icosahedral Gold Nanoclusters. *Small* **2021**, *17*, 2007992.
(38) Tofanelli, M. A.; Ackerson, C. J. Superatom Electron Configuration Predicts Thermal Stability of $Au_{25}(SR)_{18}$ Nanoclusters. *J. Am. Chem. Soc.* **2012**, *134*, 16937−16940.
(39) Compel, W. S.; Wong, O. A.; Chen, X.; Yi, C.; Geiss, R.; Häkkinen, H.; Knappenberger, K. L.; Ackerson, C. J. Dynamic Diglyme-Mediated Self-Assembly of Gold Nanocluster. *ACS Nano* **2015**, *9*, 11690−11698.
(40) Qian, H.; Zhu, M.; Andersen, U. N.; Jin, R. Facile, Large-Scale Synthesis of Dodecanethiol-Stabilized Au_{38} Clusters. *J. Phys. Chem. A* **2009**, *113*, 4281−4284.

https://doi.org/10.1021/acs.jpclett.1c02100
J. Phys. Chem. Lett. 2021, 12, 7531−7536